Kim *et al. Int J Concr Struct Mater* (2024) 18:8
https://doi.org/10.1186/s40069-023-00645-w

International Journal of Concrete Structures and Materials

RESEARCH

Open Access

Experimental and Numerical Study on the Behavior of RC Members under Combined Loads

Sangwoo Kim[1], Yeongseok Jeong[2], Minho Kwon[3] and Jinsup Kim[3*]

Abstract

In this paper, we present an investigation of the performance of reinforced concrete (RC) columns under combined bending loads and various axial forces using a finite element method (FEM) model developed with the ABAQUS finite element program, verified with actual experimental values. In the experimental study, we applied combined bending loads and various axial forces to four RC members. Two RC members were subjected to vertical cyclic loads using displacement control with 0% axial force, while the other two were tested with vertical cyclic loads, one with 10% axial force, and the other with 20% axial force. The axial force load was applied using a specially designed setup. The experimental results of the RC members include observations of final failure mode, ductility, and axial load–bending moment interaction curves (P–M correlation curves). The experimental study confirmed that as the axial force increased, cracks in the RC columns concentrated at the center of the column. The yield strength increased by 55% when the axial force ratio was 10%, and 106% when the axial force ratio was 20%. The maximum strength increased by 28% with a 10% axial force ratio, and 50% with a 20% axial force ratio. However, ductility tended to decrease as the axial force increased, reducing by 26% with a 10% axial force ratio and 60% with a 20% axial force ratio. The analytical study produced results consistent with the experimental research, showing similar numerical trends. Finally, when comparing theoretical values, experimental results, and analytical results using P–M correlation curves, we found that the experimental value has a safety rate of 18% compared to the theoretical value. The experimental and theoretical result values were similar. Therefore, it has been demonstrated experimentally and analytically that the current design has a safety value of about 18% for the performance of the actual structure.

Keywords RC column, Axial force, Bending moment, Ductility, P–M correlation curve

1 Introduction

RC columns are compression members designed to support compressive loads and transmit axial loads from top to bottom. They possess the material advantage of resisting both axial and lateral loads, such as fixed loads, transmitted from the top. However, in actual structures, RC columns rarely experience solely central compression forces. Due to the continuity of members, almost all elements like columns and arches, which primarily carry compressive forces, must also resist bending moments. Construction errors can lead to eccentricities, generating bending moments after construction, even if they were initially designed for purely axial forces.

Journal information: ISSN 1976-0485 / eISSN 2234-1315.

*Correspondence:
Jinsup Kim
jinsup.kim@gnu.ac.kr
[1] Department. of Civil Engineering, Gyeongsang National University, 501 Jinju-Daero, Jinju 52828, Republic of Korea
[2] Department of Civil Engineering, The University of Texas at Arlington, Arlington, TX 76019, USA
[3] Department. of Civil Engineering, Gyeongsang National University, Jinju 52828, Republic of Korea

Considering these various scenarios, structural members should be designed to withstand both compressive forces and bending moments simultaneously. Historically, many experimental studies have mainly focused on unidirectional loads of columns under constant axial load conditions. However, it is essential to consider seismic effects that include two horizontal component loads, which generally cause more damage than unidirectional action. Interest in the inelastic responses of axial load members with a history of biaxial bending moments has emerged relatively recently, and such conditions have become the subject of some experimental studies over the past few years (Akguzel & Pampanin, 2010; Bechtoula et al. 2005; Kim & Lee, 2000; Li et al. 2008; Monti & Nuti, 1992; Qui et al. 2002; Rodrigues et al. 2010, 2012a, 2012b, 2013; Saatcioglu & Ozcebe, 1989).

Recently, studies focusing on the behavior of RC columns under specific conditions or environmental settings are also actively pursued (Mohammadmahdi et al. 2021; Ghasem et al. 2020, 2021; Ghasem & Majid, 2019; Gautham et al. 2022; Shao et al. 2021; Alaa et al. 2022).

Additionally, research is currently underway to conduct experiments to evaluate the performance of structures and analyze the results based on the Finite Element Method (FEM). These studies aim to enhance and optimize various aspects of structural behavior, such as strength, durability, and load-carrying capacity. The experimental outcomes provide valuable insights into the real-world behavior of structures under different loading and environmental conditions. By utilizing FEM analysis, researchers can make more accurate predictions and improve the design of structures. Such research plays a crucial role in not only enhancing the safety and sustainability of structures but also driving innovative advancements in the field of architecture (Ali & Umer, 2021; Mohamed & Ali, 2021; Thamer et al. 2021).

Therefore, this study developed a finite element method (FEM) model using the ABAQUS finite element program to investigate the performance capabilities of RC columns under combined bending load and varying axial forces. The numerical results were validated against the experimental test results. As the assessment of RC columns' performance has typically focused on columns with a low-to-medium axial load ratio of less than 0.3 (Zulkifli et al. 2020; Kaish et al. 2018; Carlo et al. 2017; Yasser et al. 2022), the validated FEM models were employed to study the behavior of RC columns under higher axial forces. Lastly, the P–M correlation curve was discussed to predict the bending moment under combined bending load and different axial forces. Fig 1 shows the flowchart of this study.

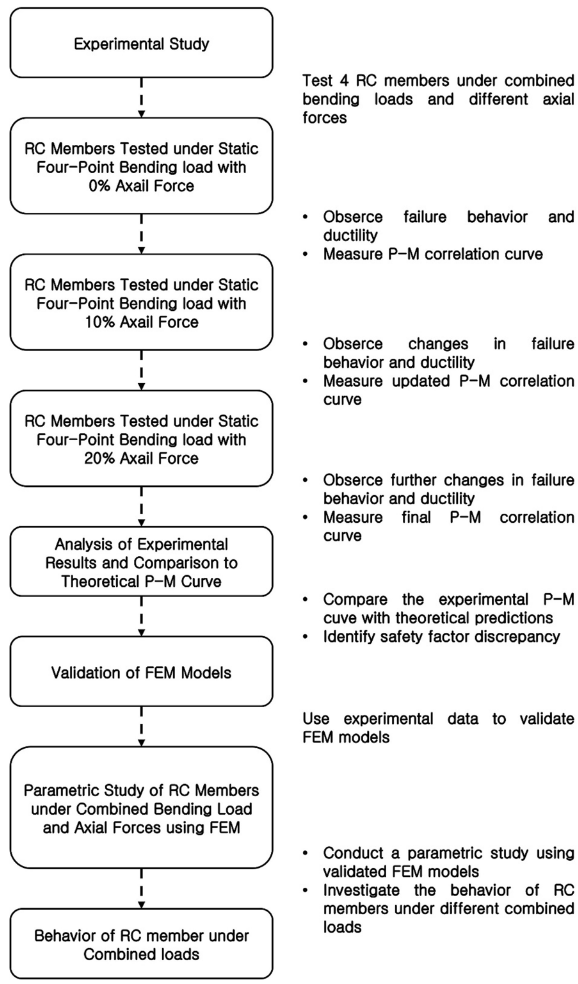

Fig.1 Flowchart

2 Experimental study

2.1 RC column

For the experiment, four RC columns were fabricated. As shown in Fig. 2, the geometric dimensions and locations of the strain gauges were identical for all RC specimens. The height of each RC column is 2400 mm, and the cross-section is 300×300 mm^2. The thickness of the concrete cover was 40 mm in all cases. The RC columns were reinforced with four longitudinal rebar with a diameter of 19 mm and eleven transverse stirrups with a diameter of 10 mm. The spacing of the transverse stirrups was 100 mm. Design of the RC columns is listed in Table 1.

Two strain gauges were attached to the longitudinal rebars of all RC specimens. Yielding of the longitudinal rebar is expected to occur at the center of the lower longitudinal rebar because the bending load direction is from the top to the bottom (as shown in Fig. 2).

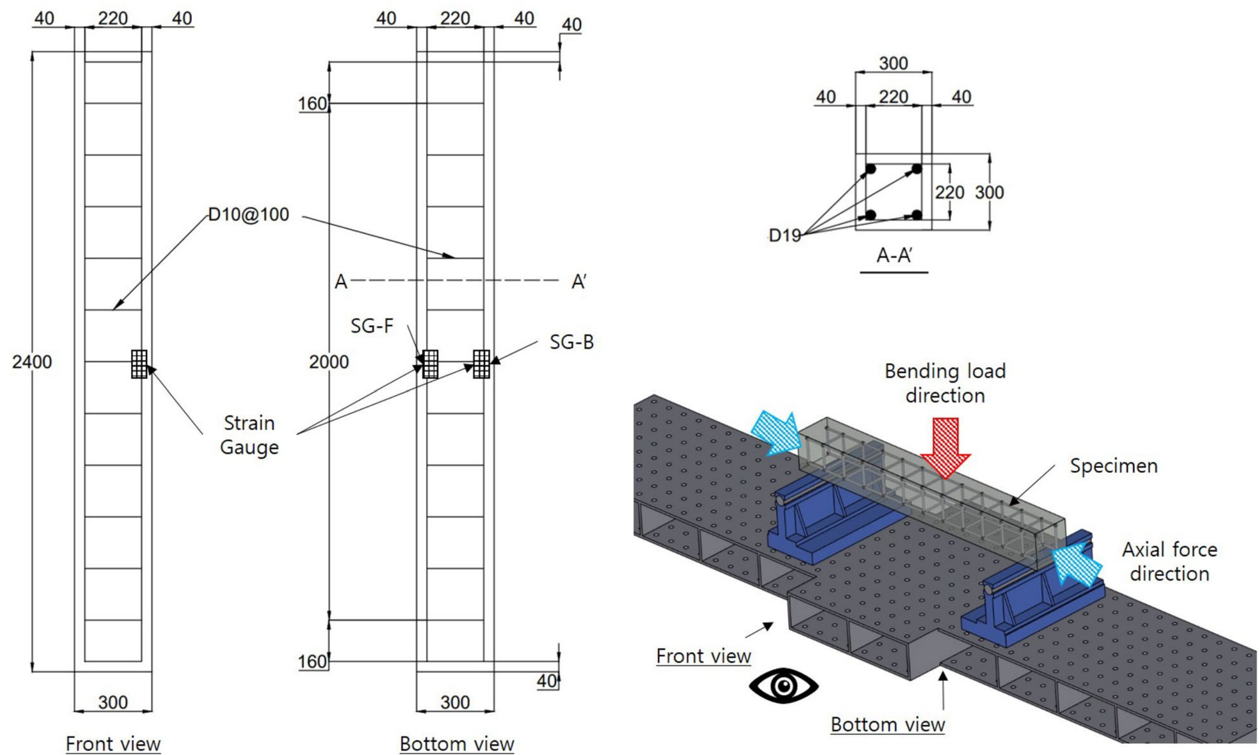

Fig. 2 Details of RC specimens and Loading direction

Table 1 Design of the RC Columns

Dimension [mm]	Length [mm]	Concrete cover [mm]	Concrete [MPa]	Longitudinal rebar [mm]	Transverse stirrup [mm]	Rebar ratio [%]
300×300	2400	40	24	19	10	1.53

Therefore, the strain gauges were attached to the center of the two longitudinal rebars, which were placed near the bottom side of the specimen. The strain gauge placed near the front view is referred to as SG-F(Front) and the other strain gauge is termed SG-B(Back). Fig 3 shows the specimen fabrication process.

2.2 Material properties

All RC columns were fabricated using the same ready-mixed concrete. The design strength of the concrete was 24 MPa. As shown in Fig. 4, three cylindrical concrete specimens (size: 100×200 mm) were fabricated with the same ready-mixed concrete which was mixed for the RC specimen. For the concrete compressive test, a 300 kN universal testing machine (UTM) was used. To measure the linear strain in the direction of the pressing force of concrete according to the compressive force, two linear variable displacement transducers (LVDT) were installed on the left and right sides of the cylindrical specimen to measure the displacement. The compressive strength of the concrete was calculated as the average strength of three cylindrical concrete specimens. Three cylindrical concrete specimens were tested after 28 days of curing in water. As a result of the compressive test, the measured average was found to be 23.9 MPa.

For reinforcement, deformed steel bars with the yield strength of 300 MPa are used for both measured longitudinal rebars and stirrups. To test the tension of the rebar, a 2000 kN universal testing machine (UTM) was used. The tension strength of the longitudinal rebars was also calculated as the average strength of three rebar tension specimens, as shown in Fig. 5. To measure the strain of the rebar tension specimens, a strain gauge was attached to the center of the rebar tension specimen. These results showed an average value of 347.3 MPa. The results from the concrete compressive strength test and the tension strength test of the rebar are provided in Fig. 6 and Table 2.

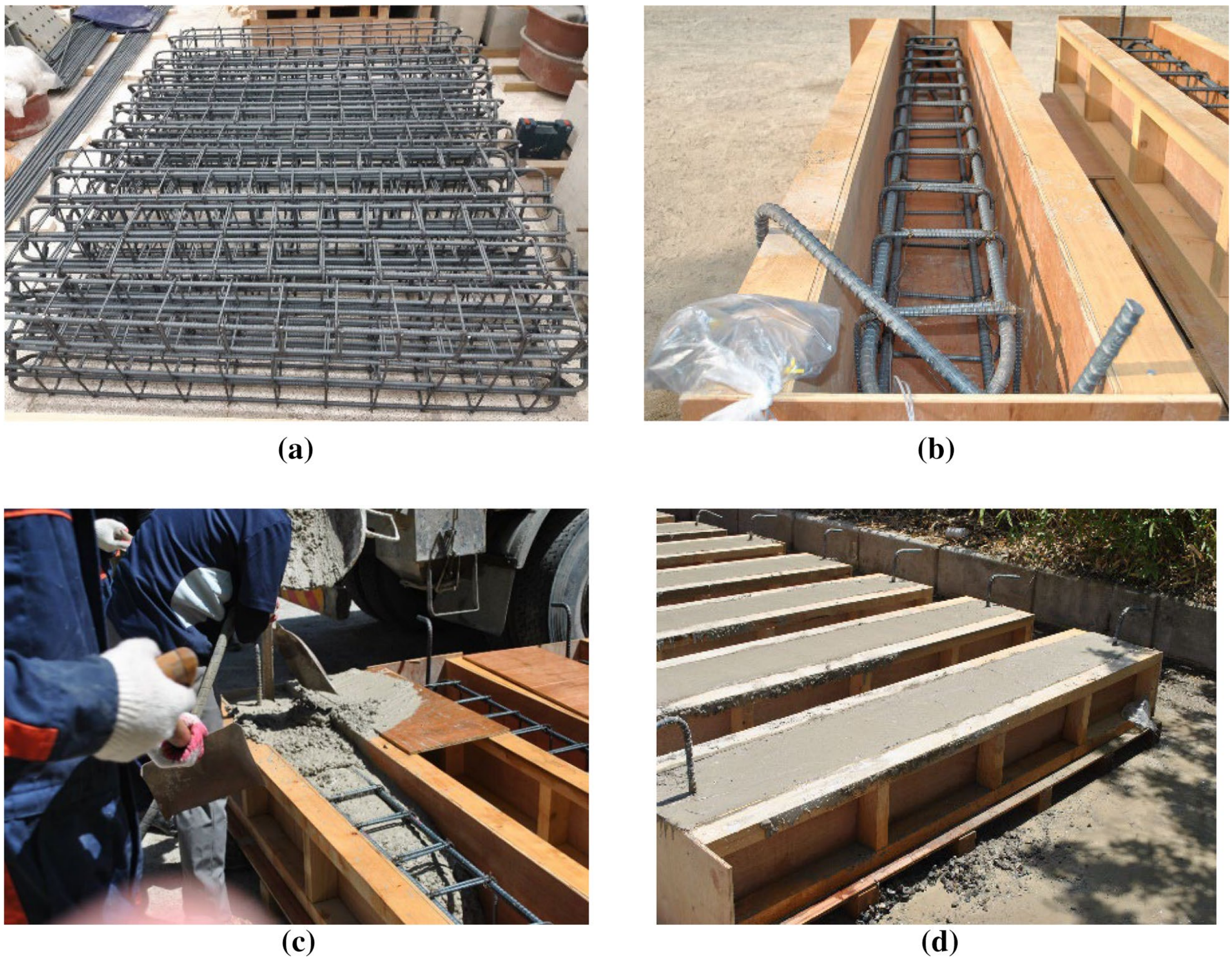

Fig. 3 Formwork of RC specimens: **a** steel rebar, **b** formwork, **c** casting, and **d** curing

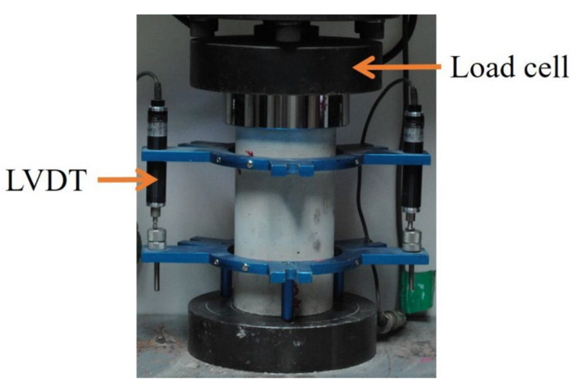

Fig. 4 Test setting for the concrete compressive test

2.3 Test setup

The process of the RC column test is shown in Fig. 7. The first step was to put the RC column on the support hinge, as shown in Fig. 8. Then, the axial forcing device was put on the RC column. The axial forcing device contains two steel beams, a 1000 kN capacity hydraulic jack, a hinge, twelve round steel bars with a diameter of 22 mm, four steel plates, and several tools, in this case bolts. As shown in Fig. 9, the axial force was transferred to the RC column via a hydraulic jack with a capacity of 1000 kN. Two steel beams placed at both ends of the RC column and the hydraulic jack are connected to the twelve round steel bars. The steel beams and the round bars were connected and fixed using steel plates and bolts. In this setup, one side of the RC column is connected to the hydraulic jack attached to a steel beam and the other side of the RC column is connected to a hinge that is attached to a steel beam. Therefore, when the hydraulic jack pushes toward the RC column, the steel beam (attached to the hydraulic jack) pushes in the opposite direction due to the law of action and reaction. Because the steel beams are connected to each other via the round steel bars, the axial force was applied to the column by self-anchoring. The

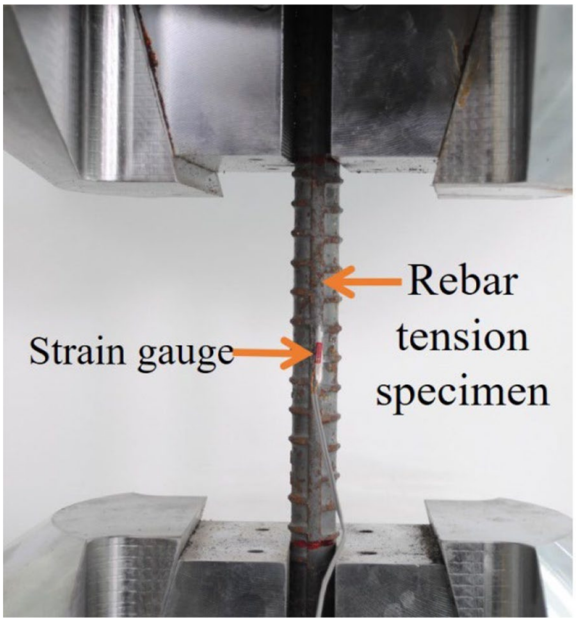

Fig. 5 Tension strength test setting for the longitudinal rebar

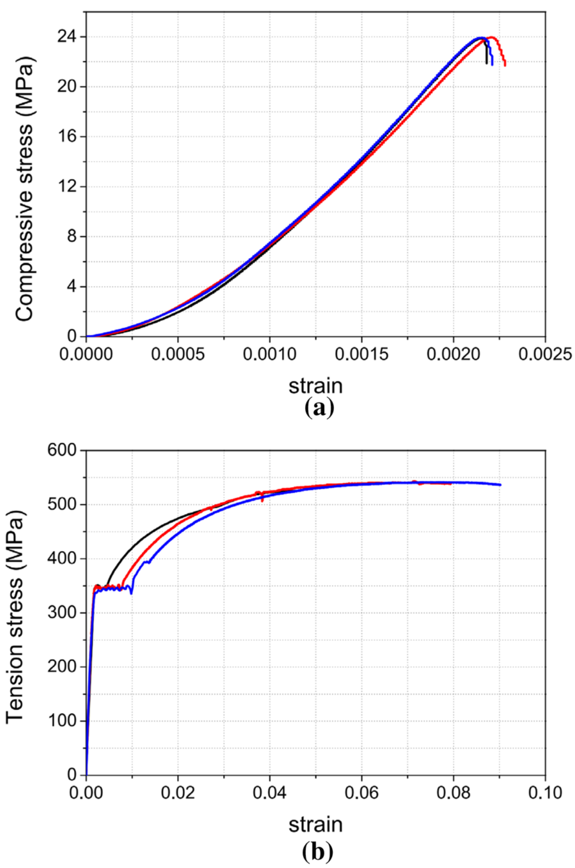

Fig. 6 Stress–strain relationship for the materials used here: **a** concrete, **b** longitudinal rebar

Table 2 Mechanical Properties of the Materials Used

Material	Yield Strength [MPa]	Yield Strain	Elastic Modulus (MPa)
Concrete	23.9	0.002	10,873
Longitudinal rebar	347.3	0.002	150,978

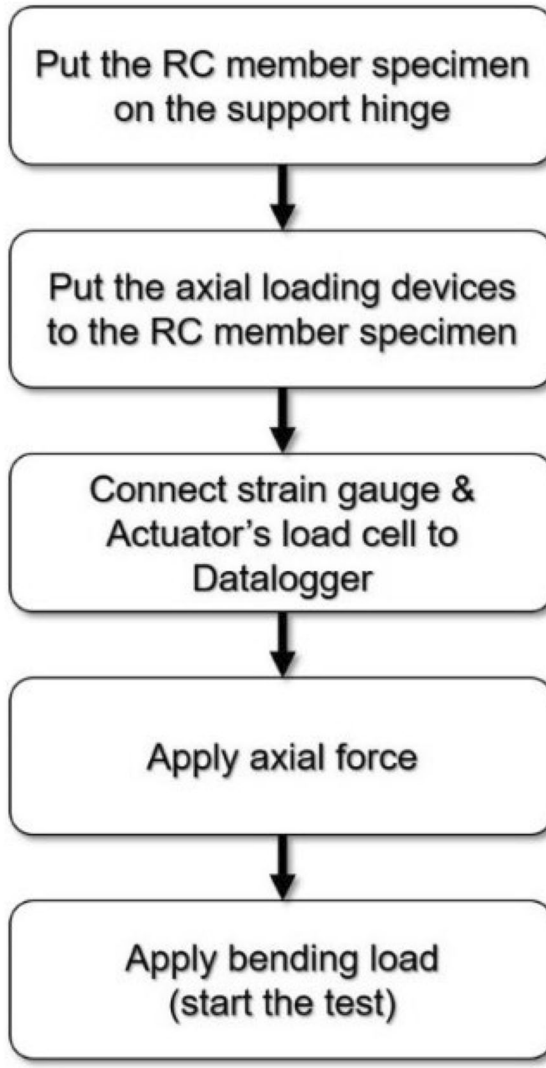

Fig. 7 Process of the RC column test

stress generated by the axial force was uniformly distributed to the round steel bars. The axial force was applied to the specimen as calculated in Table 3. For RC-A10, the magnitude of the axial load was approximately 215.3 kN and for RC-A20 it was about 430.6 kN.

For the bending load, vertical cyclic loading was applied to the column using 500kN actuator, as shown in Figs. 8 and 9. The length of the pure bending zone

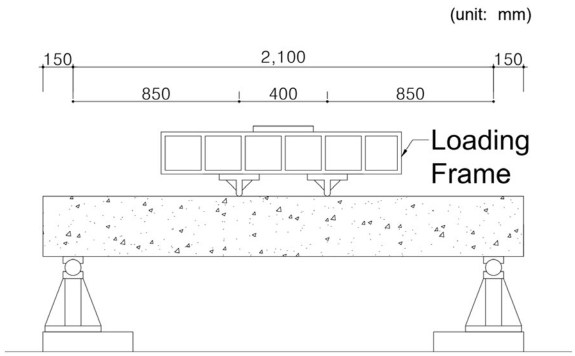

Fig. 8 Bending load diagram

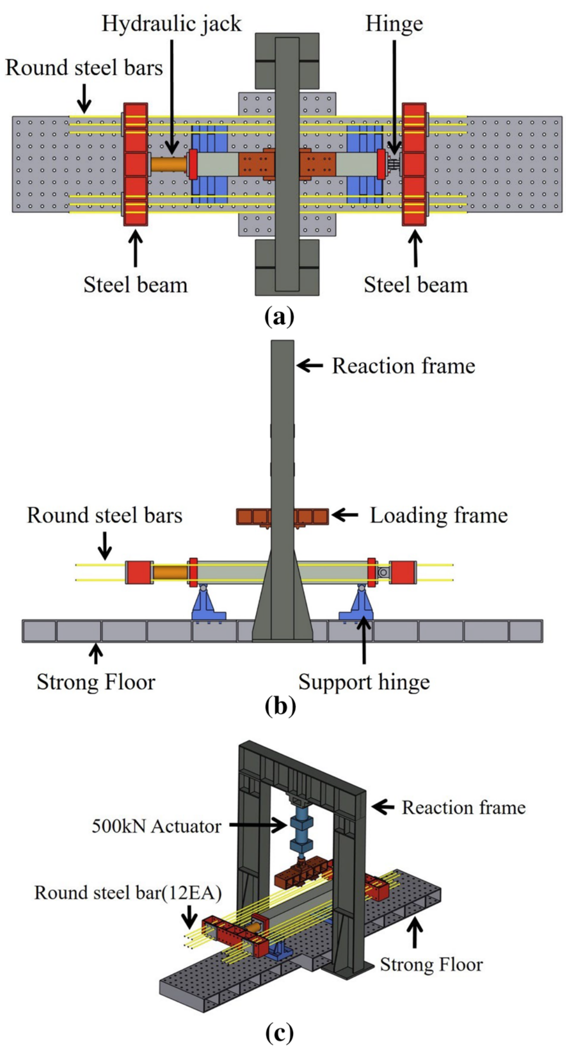

Fig. 9 Test setting for the RC column: **a** top view, **b** side view, and **c** overall view

was 400 mm, and the distance from the support hinge to the loading frame was 850 mm. The distance between the two support hinges was 2100 mm.

Table 3 Names and Parameters of RC Columns

RC Specimen	Axial force percentage, (a) [%]	Width × height, (A_g) [mm]	Concrete strength, (f_{ck}) [MPa]	Axial force [1)] [kN]
RC-A00-1	0	300 × 300	23.9	0
RC-A00-2	0			0
RC-A10	10			215.3
RC-A20	20			430.6

$a/100 \times Ag \times f_{ck}$

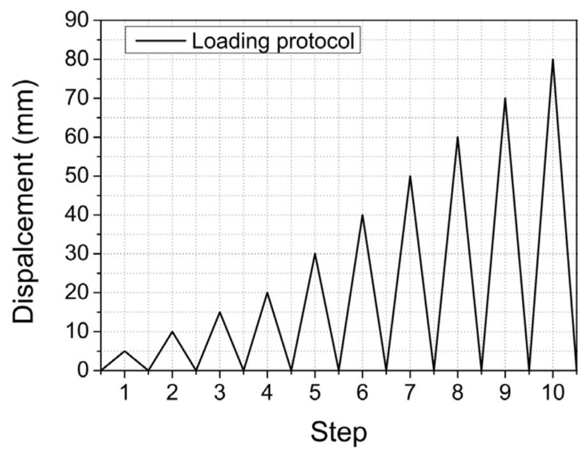

Fig. 10 Loading protocol for the bending load

As shown in Fig. 10, the vertical cyclic loading on the specimens was divided into two steps in displacement control. Before the yielding of longitudinal steel bars, with a rate of 5 mm per minute applied at each increment up to 10 mm. When the longitudinal steel bars yielded (10 mm), loading started to be performed with the displacement increment at each cycle equal to the displacement of the loading point (10 mm) at this time. The displacement increases to 80 mm.

Fig 11 shows the layout of the instrumentation used in the RC column test. The strain forces acting on the longitudinal rebars were measured with strain gauges attached along each longitudinal rebar inside the RC columns. The degree of deformation of the LVDT was measured to determine the horizontal displacement at the bending load point of the beam using a data-logger. The reaction force was measured using a load sensor positioned inside a 500-kN actuator through a 500-kN actuator controller and a data-logger.

3 Experimental test results and discussion

3.1 Final failure mode

The final failure mode and crack distribution of the RC beams are depicted in Fig. 12. All RC columns exhibited

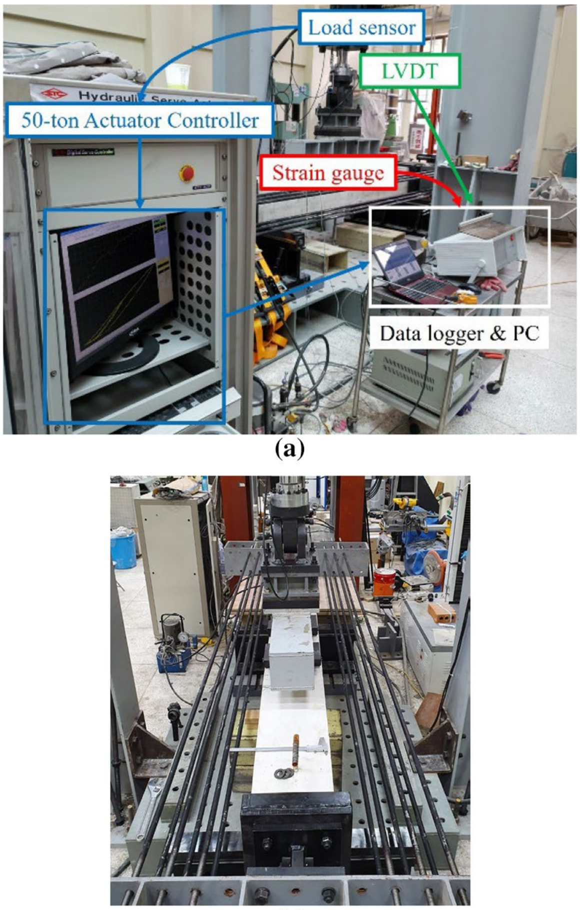

Fig. 11 Layout of the instrumentation used in the RC column test: **a** experiment equipment, **b** experimental setting

the flexural failure mode. In the absence of applied axial force (RC-A00-1 and RC-A00-2), flexural cracks were observed at the bottom of the mid-span, accompanied by concrete cover spalling due to the compressive force between the bending loading points (pure bending zone). As the axial force was increased, the concentration of flexural cracks became more prominent in the pure bending zone. Notably, for the RC-A20 specimen, concrete crushing occurred in the flexural compression area at the pure bending zone, indicating the influence of axial force on the structural response.

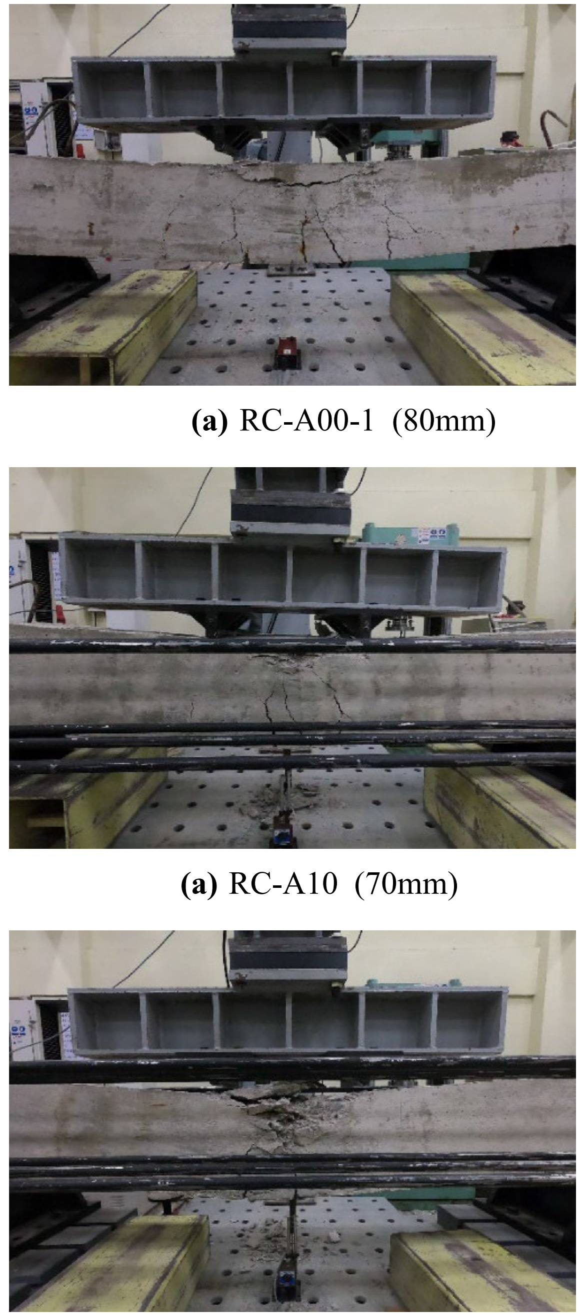

Fig. 12 Final failure mode of the RC column

3.2 Load–displacement relationship and characteristic points of envelope curves

In this study, the plastic deformation capacity of each column is measured according to the ductility ratio. With regard to the ductility, three characteristic points (i.e., yield point, peak point, and ultimate point) of each specimen are defined, as shown in Fig. 13. The yield point was calculated as the value of the strain gauge attached to the longitudinal rebar reached 0.002 (based on the results in Table 2 and Fig. 14). The peak point was defined as the point at which the specimen reached its maximum load, while the ultimate point was identified as the point at which the specimen lost 20% of its maximum load. P_y, P_p, and P_u represent the load at yield, at the peak, and at the ultimate point, respectively. Accordingly, Δ_y, Δ_p, and

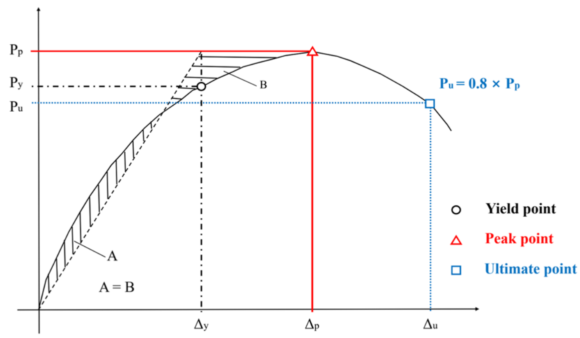

Fig. 13 Definition of the characteristic point (yield point, peak point, and ultimate point)

Δ_u represent the displacement at yield, peak, and ultimate point, respectively. Ductility was calculated as using Eq. (1). Characteristic points during the experimental test for each specimen are indicated in Fig. 15, and the corresponding values are listed in Table 4.

$$\mu = \Delta_u / \Delta_y \tag{1}$$

3.3 Load–displacement relationship and characteristic points of the envelope curves

Fig 15 shows the load–displacement (P-Δ) hysteresis and envelope curve for each specimen. RC-A00-1 reached a yield load of 108 kN at a corresponding displacement of 8.9 mm. After the yield point, RC-A00-1 reached a peak load of 159kN at a corresponding displacement of 34.6 mm. Therefore, the ultimate load is 127 kN at the corresponding displacement of 39.3 mm.

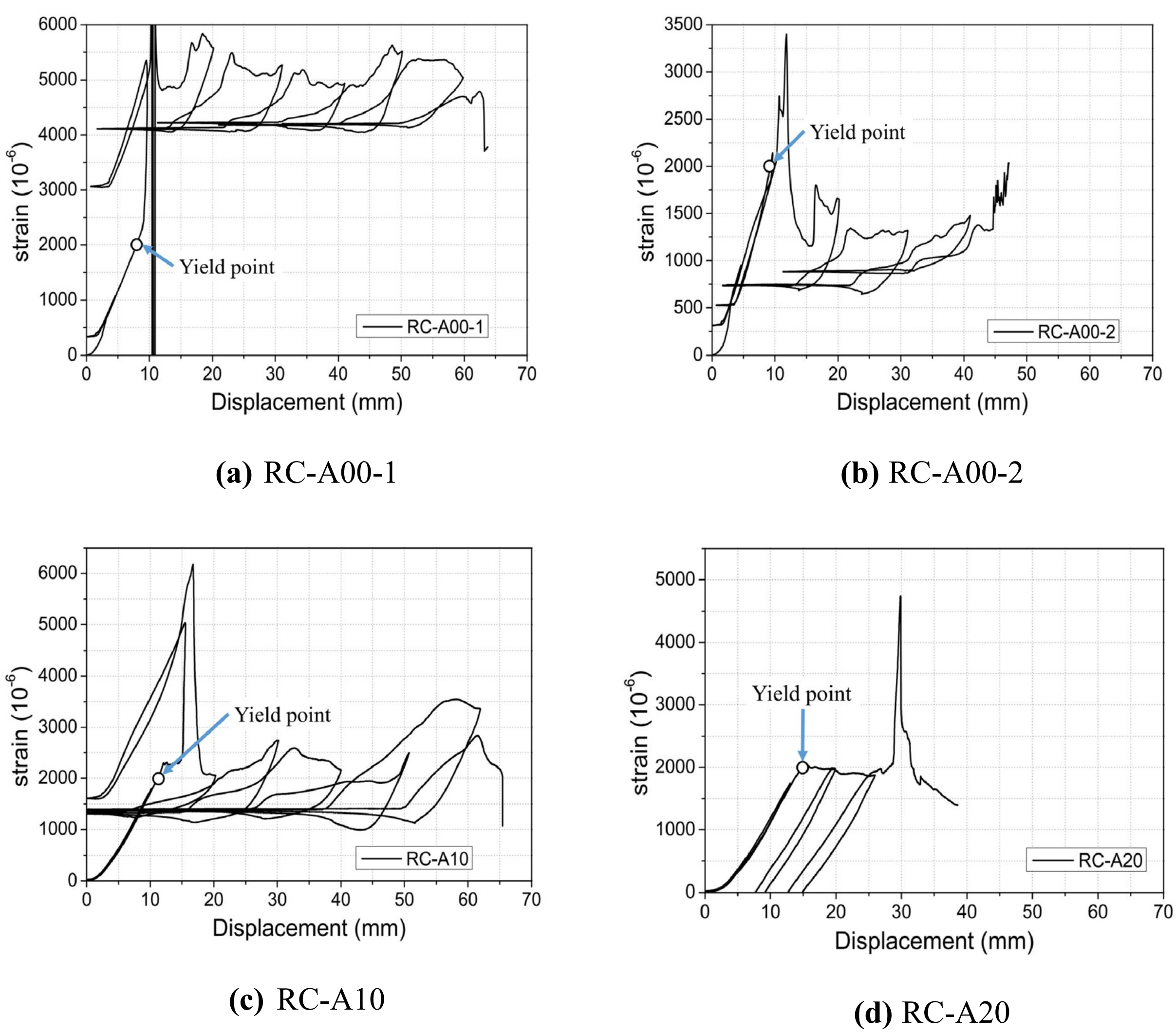

Fig. 14 Strain–displacement relationship of the longitudinal rebar

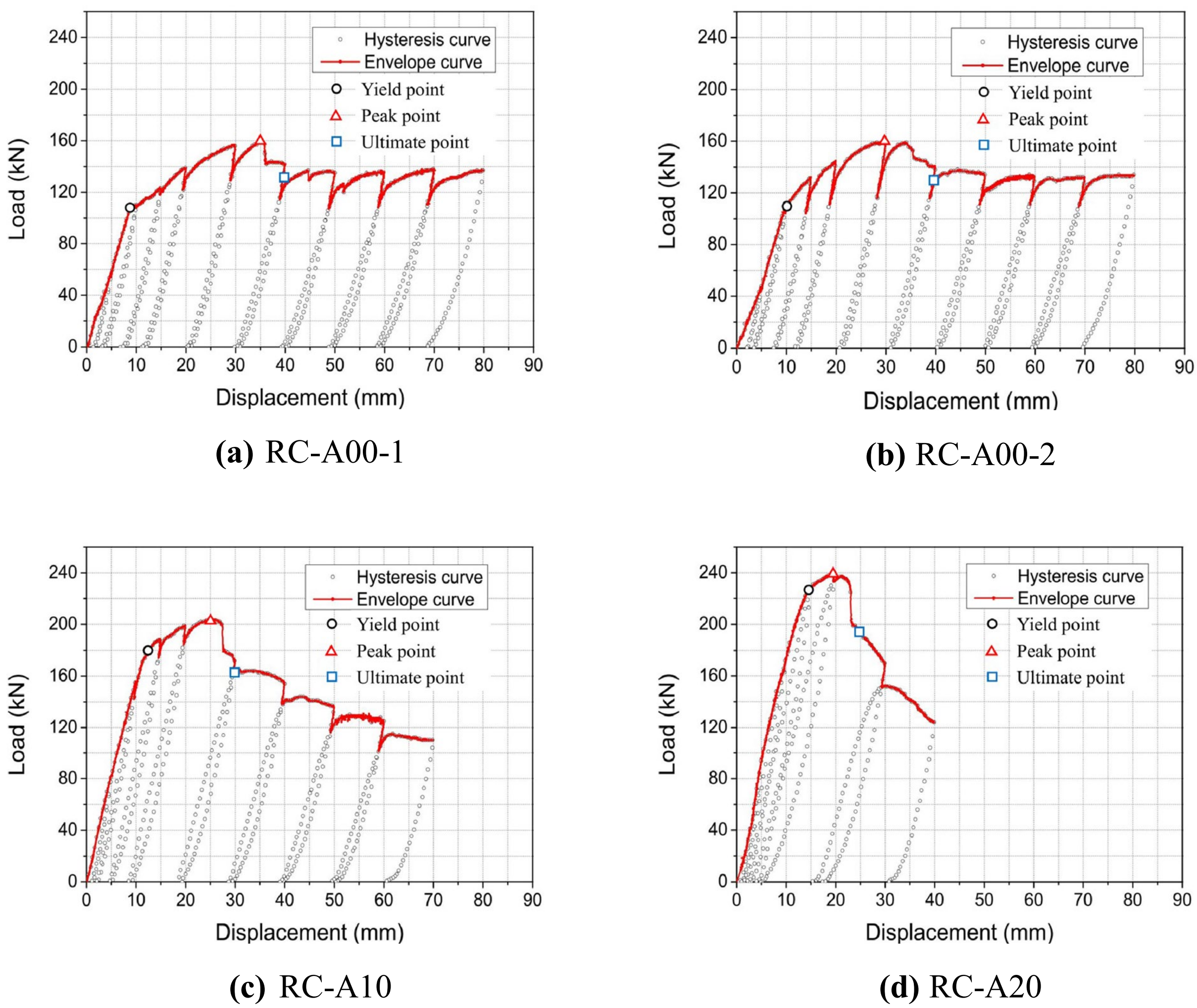

Fig. 15 Load–displacement relationship of RC columns

Table 4 Characteristic Values of the Envelope Curves

Specimen	Yield point		Peak point		Ultimate point		Ductility
	P_y [kN]	Δ_y [mm]	P_p [kN]	Δ_p [mm]	P_u [kN]	Δ_u [mm]	μ
RC-A00-1	108	8.9	159	34.6	127	39.3	4.4
RC-A00-2	111	9.9	160	29.6	128	39.5	4
RC-A10	170	11.2	204	24.7	163	30	2.7
RC-A20	226	14.9	239	18.9	191	25.3	1.7

RC-A00-2 reached a yield load of 111 kN at a corresponding displacement of 9.9 mm. After the yield point, RC-A00-2 reached a peak load of 160 kN at a corresponding displacement of 29.6 mm. Hence, the ultimate load is 128 kN at the corresponding displacement of 39.5 mm.

RC-A10 reached a yield load of 170 kN at a corresponding displacement of 11.2 mm. After the yield point, RC-A10-1 reached a peak load of 204 kN at a corresponding displacement of 24.7 mm. Hence, the ultimate load is 163 kN at the corresponding displacement of 30 mm.

RC-A20 reached a yield load of 226 kN at a corresponding displacement of 14.9 mm. After the yield point, RC-A20 reached a peak load of 239 kN at a corresponding displacement of 18.9 mm. Thus, the ultimate load is 191 kN at the corresponding displacement of 25.3 mm.

The load, displacement, and ductility were evaluated in this study. As shown in Fig. 16a, under the constraint of axial force, the load values of all characteristic points tended to increase as the axial force increased. The yield strength increased by 55% when the axial force ratio was 10% and by 106% when the axial force ratio was 20%. Similarly, the maximum strength increased by 28% with a 10% axial force ratio and by 50% with a 20% axial force ratio.

Fig 16b illustrates that as the axial force increased, the displacement of the peak point and the ultimate point tended to decrease, while the displacement of the yield point tended to increase. Due to these trends, the ductility decreased as the axial force increased, reducing by 26% with a 10% axial force ratio and by 60% with a 20% axial force ratio, as shown in Fig. 16c.

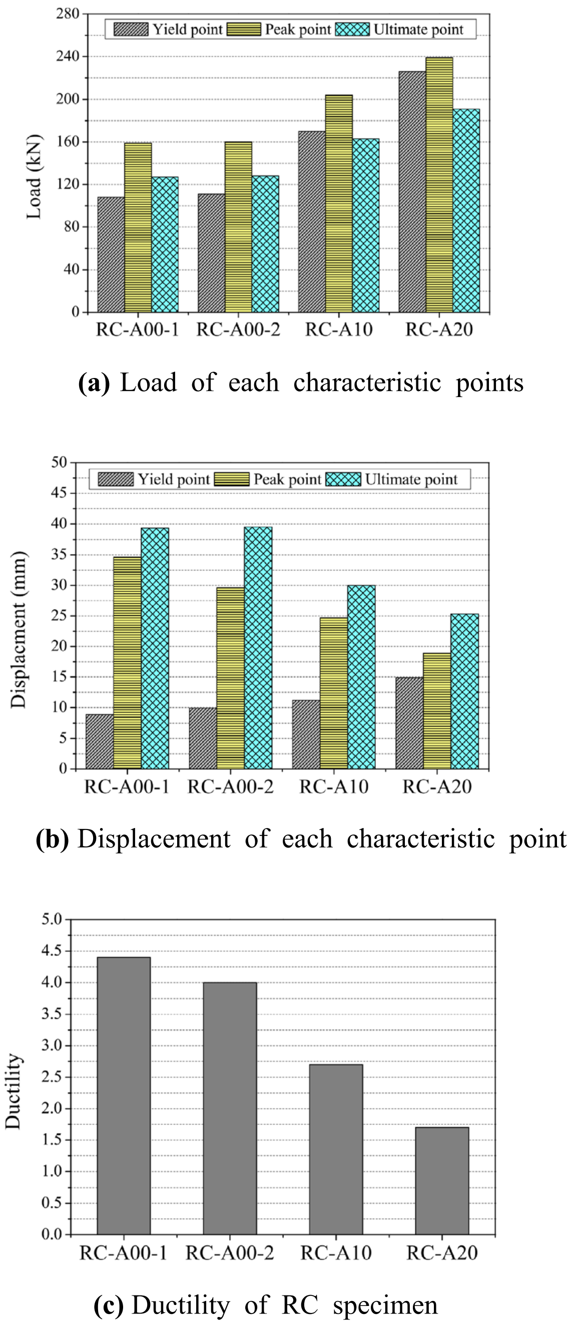

Fig. 16 Comparison of the load, displacement, and ductility outcomes of RC columns

3.4 P–M correlation curves

Fig 17 shows the theoretical P–M correlation curve of the RC column and the calibrated (with the experiment test result) P–M correlation curve. The experiment test results are shown for RC-A00, RC-A10, and RC-A20. RC-A00 is the average value of RC-A00-1 and RC-A00-2. The theoretical P–M correlation curve is based on the design code (ACI 318–19). The calibrated P–M correlation curve was derived by multiplying the value of the moment of the theoretical P–M interaction curve by 1.18. As shown in Fig. 17, the experimental values match the calibrated P–M interaction curve. Therefore, regarding the relationship between the axial load and the bending moment, these outcomes means that the actual structure has a safety factor that exceeds the theoretical value by 18%. Therefore, it has been demonstrated experimentally and analytically that the current design has a safety value of about 18% for the performance of the actual structure. Table 5 shows the results of a comparison between the theoretical P–M correlation curve and the experimental results.

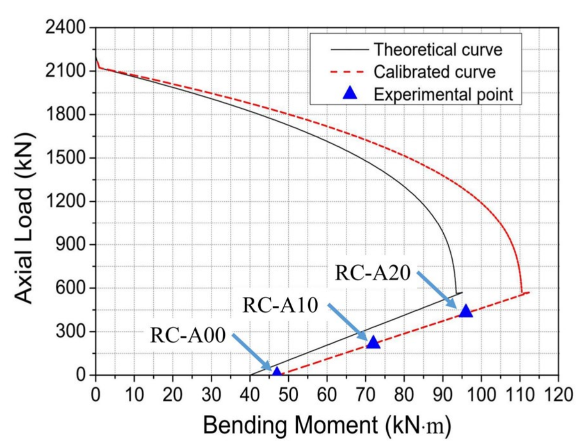

Fig. 17 P–M correlation curve

Table 5 Comparison between the Theoretical the P–M Correlation Curves and Experimental Results

Specimen	Axial Force (P) [%]	Axial Force (P) [kN]	Experimental Bending Moment (M_{exp}) [kN·m]	Theoretical Bending Moment (M_{the}) [kN·m]	Ratio (M_{exp}/M_{the})
RC-A00	0	0	46.75	39.98	1.17
RC-A10	10	215.28	72.25	60.81	1.19
RC-A20	20	430.56	96.05	81.65	1.18

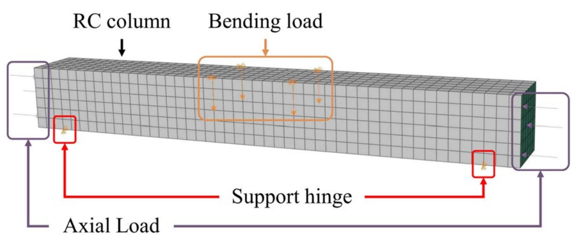

Fig. 18 FEM model of a column

3.5 Numerical study

Given that physical experiments cannot be performed in every case involving different levels of axial force, it is important to develop a FEM model capable of evaluating the performance capabilities of columns under combined bending load and different axial forces. The proposed FEM model for RC columns was verified through a comparison with results from earlier experimental studies, and the bending moment corresponding to the applied axial force was derived by applying a wider range of axial forces (0.05, 0.15, 0.3, 0.4, 0.5, 0.6) using the verified FEM model. The derived bending moments were compared with the both the theoretical and the calibrated P–M correlation curve to analyze the degree of error. The finite element program ABAQUS 6.14 was used to determine the correlation between the numerical and experimental results of columns under combined bending load and different axial forces. Fig 18 presents the entire FEM model used in the numerical study. The FEM model of the column was designed identically to that in the experimental study. After imposing an axial load, the analysis was conducted while gradually increasing the displacement.

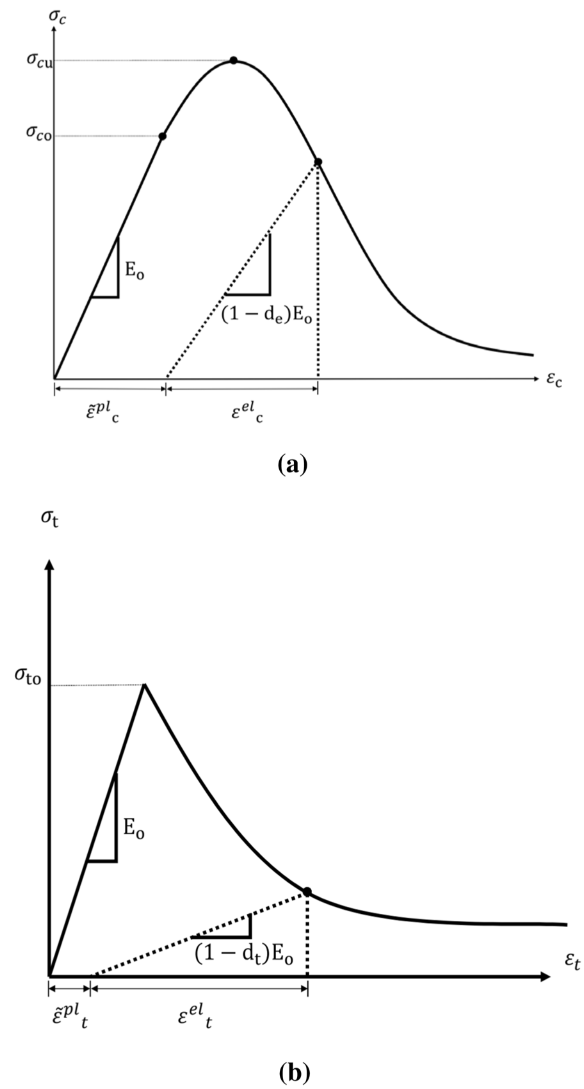

Fig. 19 Concrete damage plasticity model: **a** compressive behavior, **b** tension behavior

3.6 Material model

The concrete damaged plastics model (CDP model) as shown in Fig. 19 was used to model the solid elements of concrete so as to analyze the concrete destruction under compressed and compressed conditions. This concrete model was originally proposed by Lubliner et al. (1989) and subsequently improved by Lee and Fenves (1998). Damage Plastic models are suitable for predicting damage-plastic configurations, taking into account compression softening, plastic expansion, stiffness damage, and the tensile reinforcement properties in constrained pressure states. Truss elements are used to represent steel reinforcement and are placed at locations identical to those in the actual reinforcement

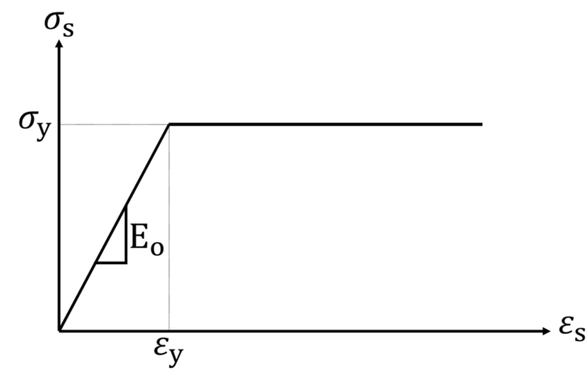

Fig. 20 Constitutive model for the steel material

Table 6 Material Properties for the Numerical Study

Material	Yield Strength [MPa]	Peak Strength [MPa]	Young's Modulus	Poisson's Ratio
Concrete	–	24	10872.7	0.2
Steel	347	536	150978.3	0.3

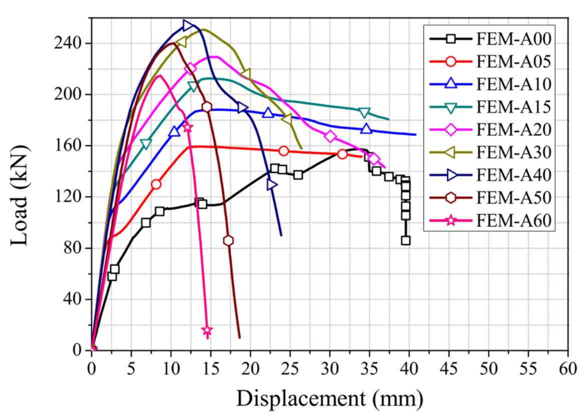

Fig. 21 Load–displacement curve of the FEM models

configurations, as shown in Fig. 2. A perfectly plastic model was used for the truss elements of the rebars considering the nonlinearity of the rebars, as shown in Fig. 20. The material properties of the FEM model are calibrated with the measured material strength values, as shown in Table 6.

3.7 Numerical study results

Fig 21 and Table 7 show the results of the numerical study. As the axial force increases, both the load and displacement of the yield points increase. When the axial force exceeds, the rebar of the RC column does not yield. In addition, as the axial force increases, the load at the peak point increases. The initial strain of the longitudinal rebar was found to be linearly proportional to the axial force.

Fig 22 and Table 8 show the results of a comparison between the outcome of the experimental study (RC-A00-1&2, RC-A10, RC-A20) and those of the numerical study (FEM-A00, FEM-A10, FEM-A20). The difference between the yield load of RC-A00-1 and that of FEM-A00 is -4 kN, and the difference in yield displacements is 2.1 mm. The difference between the peak load of RC-A00-1 and that of FEM-A00 is 1.62 kN, and the difference in the peak displacement between these two specimens is 1.6 mm. The difference between the yield load of RC-A00-2 and FEM-A00 is -1 kN, and the yield displacement difference is 1.1 mm. The difference between the peak load of RC-A00-2 and that of FEM-A00 is 2.62 kN, and the corresponding difference in the peak displacement is 3.4 mm. The difference between the yield load of RC-A10 and that of FEM-A10 is -18 kN, and the difference in the yield displacement is 2.8 mm. The difference between the peak loads of RC-A10 and FEM-A10 is 16 kN, and the difference in their peak displacements is 10.7 mm. The difference between the yield load of

Table 7 Results from the Numerical Study

Specimen	Axial Force (P) [%]	Axial Force (P) [kN]	Yield Point		Peak point		Initial stress of longitudinal rebar	
			Load (P_y) [kN]	Disp.(Δ_y) [mm]	Load (P_p) [kN]	Disp. (Δ_p) [mm]	Value	Ratio
FEM-A00	0	0	112	11	157.38	33	0	
FEM-A05	5	107.64	159	13	159	13	8.44	1
FEM-A10	10	215.28	188	14	188	14	16.88	2
FEM-A15	15	322.92	212	14	212	14	25.32	3
FEM-A20	20	430.56	229	16	229	16	33.76	4
FEM-A30	30	645.84	–	–	250	14	50.64	6
FEM-A40	40	861.12	–	–	254	13	67.52	8
FEM-A50	50	1076.4	–	–	240	10	84.49	10
FEM-A60	60	1291.68	–	–	215	9	115.43	14

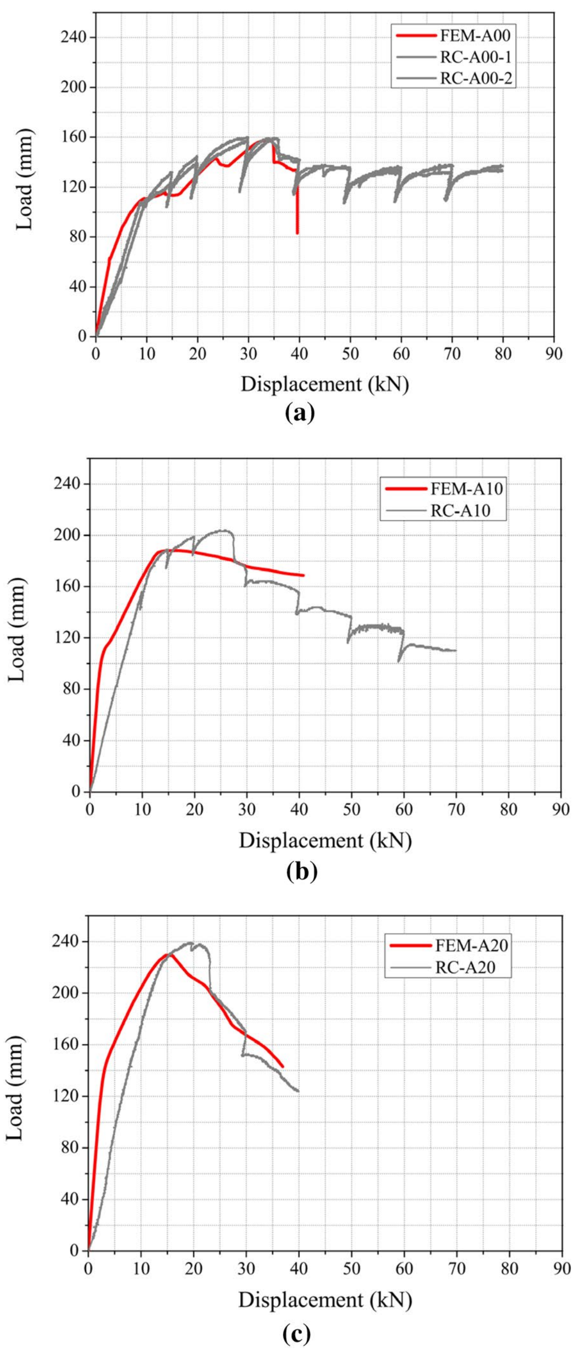

Fig. 22 Comparison of the load–displacement curves between the experimental study and the numerical study: **a** FEM-A00, **b** FEM-A10, and **c** FEM- A20

RC-A20 and that of FEM-A20 is − 3 kN, with a difference in the yield displacement of − 1.1 mm in this case. Finally, the difference between the peak load of RC-A20 and that of FEM-A20 is 10 kN, and the difference in the peak displacement is 2.9 mm. Fig 23 shows a comparison of the strain–displacement curves between the experimental study and the numerical study. The difference in this case is slight.

The overall trend suggests that the FEM model tends to predict higher bending moments in the RC columns compared to the theoretical predictions. The difference between the FEM curve and the calibrated curve is small, indicating that the FEM model can be adjusted to match the experimental results more closely.

3.8 P–M correlation curves from the numerical study

Fig 24 and Table 9 shows the results of a comparison between the P–M correlation curve from the numerical study (FEM curve) and the P–M correlation curve from the experimental study (theoretical curve vs. the calibrated curve). When the axial load equals 0%, the difference between the bending moment of the theoretical curve and that of the FEM curve is –19.1%, and the difference between the bending moment of the calibrated curve and that of the FEM curve is -0.9%. When the axial load equals 5%, the difference between the bending moment of the theoretical curve and that of the FEM curve is –34.1%, and the difference between the bending moment of the calibrated curve and that of the FEM curve is –13.6%. At an axial load of 10%, the difference between the bending moment of the theoretical curve and that of the FEM curve is − 31.4%, and the difference between the bending moment of the calibrated curve and that of the FEM curve is − 11.3%. When the axial load equals 15%, the difference between the bending moment of the theoretical curve and that of the FEM curve is − 26.5%, and the difference between the bending moment of the calibrated curve and that of the FEM curve is − 7.2%. At an axial load of 20%, the difference between the bending moment of the theoretical curve and that of the FEM curve is − 19.2%, and the difference between the bending moment of the calibrated curve and that of the FEM curve is − 1.0%. When the axial load equals 30%, the difference between the bending moment of the theoretical curve and that of the FEM curve is − 14.0%, and the difference between the bending moment of the calibrated curve and that of the FEM curve is 3.4%. At an axial load of 40%, the difference between the bending moment of the theoretical curve and that of the FEM curve is − 17.5%, and the difference between the bending moment of the calibrated curve and that of the FEM curve is 0.4%. Additionally, when the axial load equals 50%, the difference between the bending moment of the theoretical curve and that of the FEM curve is − 15.9%, and the difference between the bending moment of the calibrated curve and that of the FEM curve is 1.8%. In the 60% axial load case, the difference between the bending moment of the theoretical curve and that of the FEM curve is –13.5%, and the difference between the bending

Table 8 Comparison between the FEM Model and the Experimental Results: Yield Point and Peak Point

Specimen	Yield point		Peak point	
	Load (P_y) [kN]	Disp. (Δ_y) [mm]	Load (P_p) [kN]	Disp. (Δ_p) [mm]
RC-A00-1	108	8.9	159	34.6
FEM-A00	112	11	157.38	33
Error	− 4	− 2.1	1.62	1.6
RC-A00-2	111	9.9	160	29.6
FEM-A00	112	11	157.38	33
Error	− 1	− 1.1	2.62	− 3.4
RC-A10	170	11.2	204	24.7
FEM-A10	188	14	188	14
Error	− 18	− 2.8	16	10.7
RC-A20	226	14.9	239	18.9
FEM-A20	229	16	229	16
Error	− 3	− 1.1	10	2.9

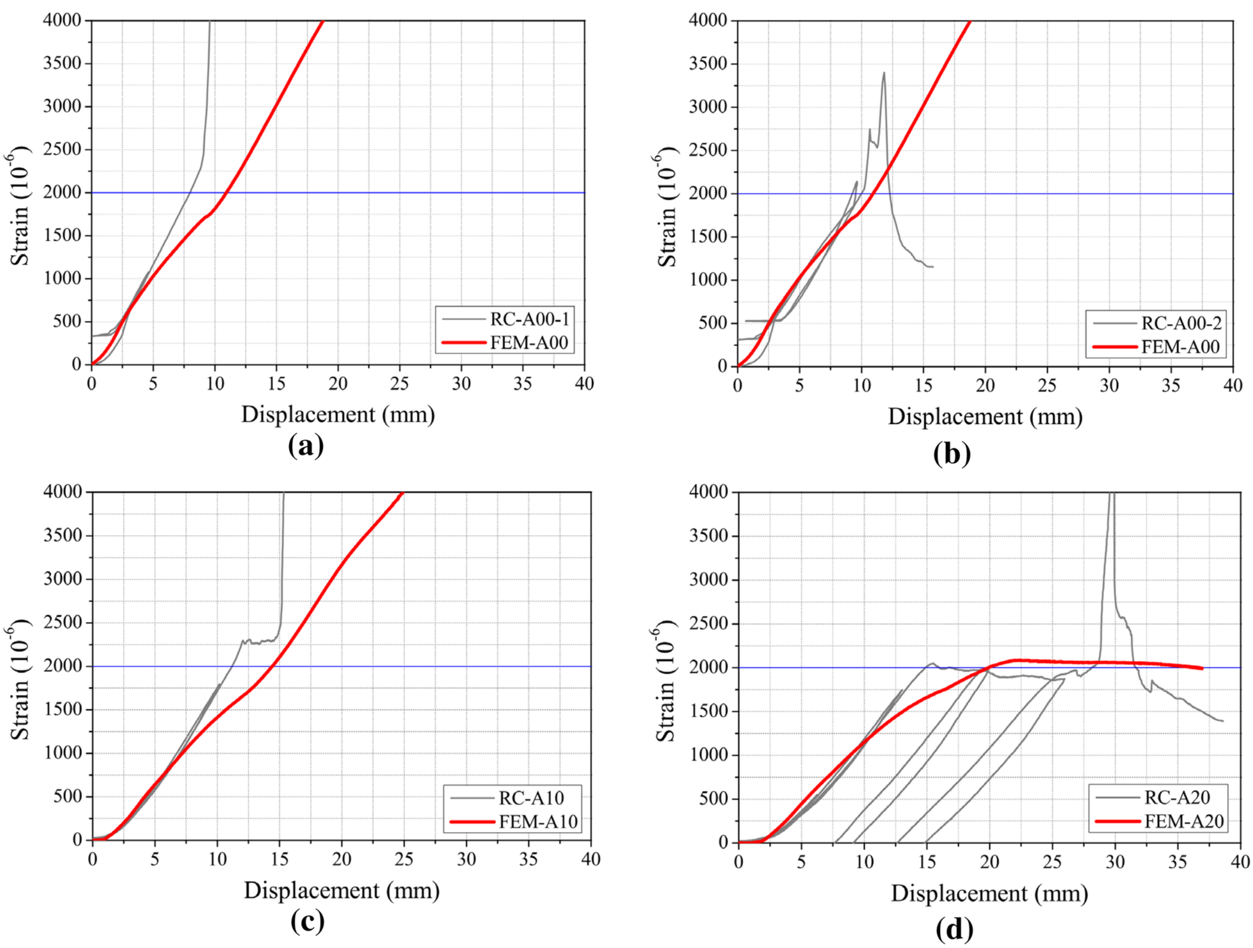

Fig. 23 Comparison of the strain–displacement curves between the experimental study and the numerical study: **a** FEM-A00-1, **b** FEM-A00-2, **c** FEM-A10, and **d** FEM- A20

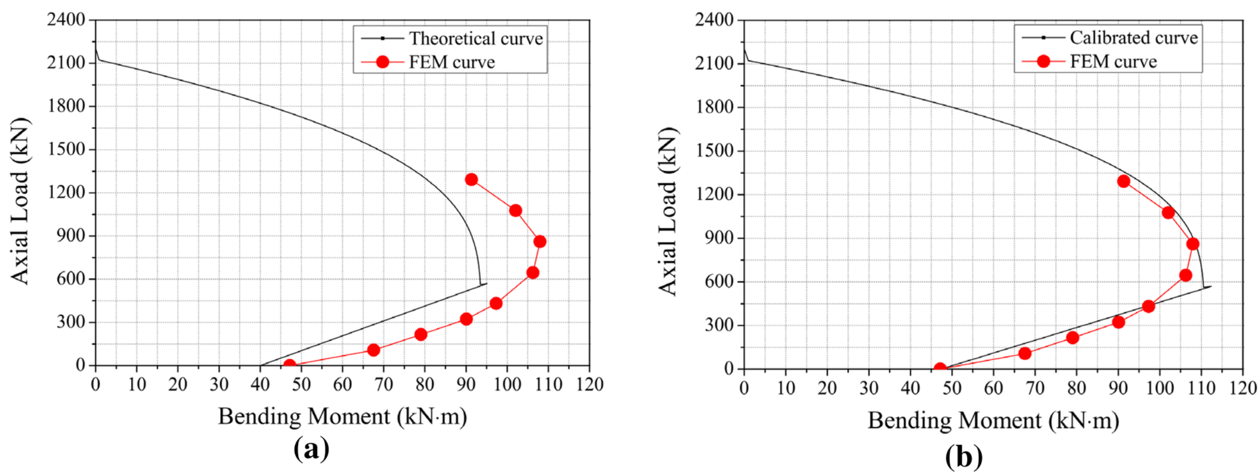

Fig. 24 Comparison of the axial load-bending moment curves: **a** theoretical curve and FEM curve, and **b** calibrated curve and FEM curve

Table 9 Comparison between the FEM Model and Experimental Study: Bending Moment

Axial Force		**Bending moment**			
[%]	**[kN]**	**Theoretical and calibrated value [kN·m]**		**FEM model [kN·m]**	**Error [%]**
0	0	Theo	39.98	47.60	– 19.1
		Cali	47.18		– 0.9
5	107.64	Theo	50.40	67.58	– 34.1
		Cali	59.47		– 13.6
10	215.28	Theo	60.81	79.90	– 31.4
		Cali	71.76		– 11.3
15	322.92	Theo	71.23	90.10	– 26.5
		Cali	84.05		– 7.2
20	430.56	Theo	81.65	97.33	– 19.2
		Cali	96.35		– 1.0
30	645.84	Theo	93.24	106.25	– 14.0
		Cali	110.02		3.4
40	861.12	Theo	91.84	107.95	– 17.5
		Cali	108.37		0.4
50	1076.4	Theo	88.02	102.00	– 15.9
		Cali	103.86		1.8
60	1291.68	Theo	80.49	91.38	– 13.5
		Cali	94.98		3.8

moment of the calibrated curve and that of the FEM curve is 3.8%. Overall, the bending moments of the FEM curves are higher than bending moments of the theoretical curves. The difference between the FEM curve and the calibrated curve is slight. The error between the calibrated curve and the FEM curve is negative up to an axial load of 20% and positive when the axial load exceeds 20%.

4 Conclusion

This study focused on investigating the effect of increasing axial force on RC columns subjected to both axial force and bending moment. Another objective was to assess the performance of reinforced concrete RC columns under combined bending loads and various axial forces using a finite element method. Based on the experimental results, the following conclusions were drawn:

The load-carrying capacity of RC columns increased with higher axial force ratios. Specifically, the yield strength and maximum strength showed significant improvements, increasing by 55% and 28%, respectively, with a 10% axial force ratio, and by 106% and 50%, respectively, with a 20% axial force ratio.

As the axial force increased, the displacement at the peak point and the ultimate point decreased, while the displacement at the yield point increased. This behavior resulted in a reduction in ductility with higher axial force ratios, showing a decrease of 26% with a 10% axial force ratio and 60% with a 20% axial force ratio.

By comparing theoretical values, experimental results, and analytical results using P–M correlation curves, it was observed that the experimental values had a safety margin of approximately 18% compared to the theoretical values. The experimental and theoretical results showed close agreement. Thus, it was experimentally and analytically demonstrated that the current design provided a safety margin of about 18% for the performance of the actual structure.

FEM model generally overestimates the bending moments in RC columns compared to the theoretical predictions. However, the calibration process shows promising results, as the difference between the FEM curve and the calibrated curve is small, indicating that the FEM model can be adjusted to achieve a closer match with experimental results. Further refinement and calibration of the FEM model could enhance its accuracy in predicting the behavior of RC columns under combined loading conditions.

The limitations of this study include a limited sample size, with only four RC members tested, as well as simplified loading conditions, using static loading instead of dynamic events. Potential material variations were not fully accounted for, and certain assumptions were made in the FEM analysis. Additionally, the study employed simplified boundary conditions and faced challenges related to scale effects and material modeling. Despite these limitations, the research provides valuable insights into the behavior of RC members under combined loading conditions and lays the groundwork for further research and improvements in structural design.

Based on the limitations of this study, several plans for future research can be considered to overcome these limitations and advance further. These plans include: (1) Expanding the sample size to consider a wider range of situations, (2) Incorporating diverse loading conditions, (3) Conducting dynamic testing to assess real-life responses, (4) Considering material variability in experiments and modeling, (5) Improving nonlinear modeling techniques, (6) Investigating larger-scale structures to account for scale effects, and (7) Evaluating various connections and reinforcements for more realistic scenarios. These plans aim to enhance the reliability and practicality of knowledge in the field of RC member behavior under combined loading conditions.

Acknowledgements
This work was supported by a grant by the Korea Agency for Infrastructure Technology Advancement (KAIA) and funded by the Ministry of Land, Infrastructure, and Transport (Grant 21SCIP-B146946-04).

Author contributions
SK contributed to conducting the experimental test, numerical study, analysis of the test results, and drafted the manuscript. YJ contributed to conducting the experimental test. MK contributed to revising the manuscript deeply. JK contributed to the conception, design of the work, and revised the manuscript. All authors read and approved the final manuscript.

Funding
This work was supported by a grant by the Korea Agency for Infrastructure Technology Advancement (KAIA) and funded by the Ministry of Land, Infrastructure, and Transport (Grant 21SCIP-B146946-04).

Availability of data and materials
All data are provided in full in the results of this paper.

Declarations

Ethics approval and consent to participate
Not applicable.

Consent for publication
Not applicable.

Competing interests
The authors declare that they have no competing interests.

Received: 30 April 2023 Accepted: 7 September 2023
Published online: 01 February 2024

References

ABAQUS. (2011). Theory and user's manual. Pawtucket (Rhode Island, USA): Hibbitt, Karlsson, and Sorensen Inc.

Akguzel, U., & Pampanin, S. (2010). Effects of variation of axial load and bidirectional loading on seismic performance of GFRP retrofitted reinforced concrete exterior beam-column joints. *Journal of Composites for Construction, 14*, 94–104. https://doi.org/10.1061/(ASCE)1090-0268(2010)14:1(94)

Ali, R., & Umer, R. (2021). Efficiency of GFRP bars and hoops in recycled aggregate concrete columns: Experimental and numerical study. *Composite Structures, 255*, 112986. https://doi.org/10.1016/j.compstruct.2020.112986

American Concrete Institute. (2012). *Building Code Requirements for Reinforced Concrete (ACI 318)*. Michigan, USA: Farmington Hills.

Bechtoula, H., Kono, S., & Watanabe, F. (2005). Experimental and analytical investigations of seismic performance of cantilever reinforced concrete columns under varying transverse and axial loads. *J Asian Archit Build Eng, 4*, 467–474. https://doi.org/10.3130/jaabe.4.467

Carlo, F. D., Meda, A., & Rinaldi, Z. (2017). Numerical evaluation of the corrosion influence on the cyclic behaviour of RC columns. *Engineering Structures, 153*, 264–278. https://doi.org/10.1016/j.engstruct.2017.10.020

Gautham, A., & Sahoo, D. R. (2022). Performance of SRC column-RC beam joints under combined axial and cyclic lateral loadings. *Engineering Structures, 260*, 114218. https://doi.org/10.1016/j.engstruct.2022.114218

Ghasem, P., & Majid, G. (2019). Evaluation of concrete filled steel tube column confined with FRP. *Journal of Testing and Evaluation, 48*(6), 4343–4354.

Ghasem, P., Majid, G., & Amin, M. (2020). An Experimental Study on Cyclic Performance of the Geometrically Prismatic Concrete-Filled Double Skin Steel Tubular (CFDST) Columns. *Iranian Journal of Science and Technology, Transactions of Civil Engineering., 45*, 629–638. https://doi.org/10.1007/s40996-020-00410-z

Ghasem, P., Majid, G., & Amin, M. (2021). Impact of temperature rise on the seismic performance of concrete-filled double skin steel columns with prismatic geometry. *Journal of Testing and Evaluation, 49*(4), 20200037. https://doi.org/10.1520/JTE20200037

Kaish, A. B. M. A., Jamil, M., Raman, S. N., Zain, M. F. M., & Nahar, L. (2018). (2018) Ferrocement composites for strengthening of concrete columns: a review. *Construction Build Materials., 160*, 326–340. https://doi.org/10.1016/j.conbuildmat.2017.11.054

Kim, J. K., & Lee, S. S. (2000). The behaviour of reinforced concrete columns subjected to axial force and biaxial bending. *Engineering Structures, 23*, 1518–1528. https://doi.org/10.1016/S0141-0296(99)00090-5

Lee, J., & Fenves, G. L. (1998). (1998) Plastic-damage model for cyclic loading of concrete structures. *Journal of Engineering Mechanics, 124*(8), 892–900. https://doi.org/10.1061/(ASCE)0733-9399124:8(892)

Li, L., Mander, J. B., & Dhakal, R. P. (2008). Bidirectional cyclic loading experiment on a 3D beam-column joint designed for damage avoidance. *Journal of the Structural Engineering. American Society of Civil Engineers, 134*, 1733–1742. https://doi.org/10.1061/(ASCE)0733-9445(2008)134:11(1733)

Lubliner, J., Oliver, J., Oller, S., & Onate, E. (1989). A plastic-damage model for concrete. *International Journal of Solids and Structures, 25*(3), 229–326. https://doi.org/10.1016/0020-7683(89)90050-4

Mohamed, H. E. O., & Ali, R. (2021). Data-driven analysis of concrete-filled steel-tube CFRP-confined NSC columns. *Mechanics of Advanced Materials and Structures, 29*(27), 5667–5688. https://doi.org/10.1080/15376494.2021.1961953

Mohammadmahdi, E., Masoume, H., Milad, S., Fatemeh, A., Mohammad, Y., & Ghasem, P. (2021). Experimental investigation of residual flexural capacity of damaged reinforced concrete beams exposed to elevated temperatures. *Engineering Structures, 240*, 112388. https://doi.org/10.1016/j.engstruct.2021.112388

Monti, G., & Nuti, C. (1992). Nonlinear cyclic behavior of reinforcing bars including buckling. *J Struct Eng-ASCE, 118*, 3268–3284. https://doi.org/10.1061/(ASCE)0733-9445(1992)118:12(3268)
Qiu, F., Li, W., Pan, P., & Qian, J. (2002). Experimental tests on RC columns under biaxial quasi-static loading. *Engrg Structures, 24*, 419–428. https://doi.org/10.1016/S0141-0296(01)00108-0
Rodrigues, H., Arêde, A., Varum, H., & Costa, A. G. (2013). Experimental evaluation of rectangular reinforced concrete column behaviour under biaxial cyclic loading. *Earthquake Eng Struc, 42*(2), 239–259. https://doi.org/10.1002/eqe.2205
Rodrigues, H., Varum, H., Arêde, A., & Costa, A. (2012a). A comparative analysis of energy dissipation and equivalent viscous damping of RC columns subjected to uniaxial and biaxial loading. *Engineering Structures, 35*, 149–164. https://doi.org/10.1016/j.engstruct.2011.11.014
Rodrigues, H., Varum, H., Arêde, A., & Costa, A. (2012b). Comparative efficiency analysis of different nonlinear modelling strategies to simulate the biaxial response of RC columns. *Earthq Eng Eng Vibrat, 11*, 553–566. https://doi.org/10.1007/s11803-012-0141-1
Rodrigues, H., Varum, H., & Costa, A. (2010). Simplified macro-model for infill masonry panels. *Journal of Earthquake Engineering, 14*, 390–416. https://doi.org/10.1080/13632460903086044
Saatcioglu, M., & Ozcebe, G. (1989). Response of reinforced concrete columns to simulated seismic loading. *ACI Structural Journal, 86*, 3–12. https://doi.org/10.14359/2607
Selmy, Y. M., & El-Salakawy, E. F. (2022). Numerical investigation on the seismic behaviour of GFRP-reinforced concrete rectangular columns. *Engineering Structures, 262*, 114355. https://doi.org/10.1016/j.engstruct.2022.114355
Shao, Y., Kuo, C. W., & Hung, C. C. (2021). Seismic performance of full-scale UHPC-jacket-strengthened RC columns under high axial loads. *Engineering Structures, 243*, 112657. https://doi.org/10.1016/j.engstruct.2021.112657
Swesi, A. O., Cotsovos, D. M., & Dimitri, V. V. (2022). Effect of CFRP strengthening on response of RC columns to lateral static and impact loads. *Composite Structures, 287*, 115356. https://doi.org/10.1016/j.compstruct.2022.115356
Thamer, A., Ali, R., & Nabil, B. K. (2021). Experiments and numerical simulations of glass fiber reinforced polymers in structural fibers RC members. *Mechanics of Advanced Materials and Structures., 29*(27), 6891–6906. https://doi.org/10.1080/15376494.2021.1986870
Thermou, G. E., Papanikolaou, V. K., & Hajirasouliha, I. (2021). Structural performance of RC columns retrofitted with steel-reinforced grout jackets under combined axial and lateral loading. *Engineering Structures, 245*, 112946. https://doi.org/10.1016/j.engstruct.2021.112946
Zulkifli, S., Hisbany, M. M., Ismail, R., Zakwan, F., Hazrina, A., & Ismail, B. N. (2020). Application of shape memory alloys (SMA) as a retrofit and strengthening component on reinforced concrete columns. *Journal of Physics: Conference Series: IOP Publishing, 2020*, 042104. https://doi.org/10.1088/1742-6596/1529/4/042104

Publisher's Note

Sangwoo Kim Ph.D. candidate at the Department of Civil Engineering, Gyeongsang National University, Republic of Korea

Yeongseok Jeong Post-Doctoral Research Associate at the Department of Civil Engineering, University of Texas at Arlington, USA

Minho Kwon Professor at the Department of Civil Engineering, Gyeongsang National University, Republic of Korea

Jinsup Kim Associate Professor at the Department of Civil Engineering, Gyeongsang National University, Republic of Korea